Supporting information

Superior Oxygen Reduction on Curved Fe-N_4 Sites Enabled by Molecular Infiltration within Self-Assembled Fullerene Microbelts

Fancang Meng,[a] Huan Wu,[a] Boyu Jia,[a] Kexiang Li,[a] Zhihua Wang,[a] He Zhu,[a] Chao Chen,[b,] Qingmin Ji[a,]**

[a] Herbert Gleiter Institute for Nanoscience, School of Materials Science and Engineering, Nanjing University of Science & Technology, 200 Xiaolingwei, Nanjing, 210094, China

[b] State Key Laboratory of Rare Earth Resource Utilization, Changchun Institute of Applied Chemistry, Chinese Academy of Sciences, Changchun, China.

*Corresponding author: jiqingmin@njust.edu.cn, chaochen@ciac.ac.cn

Other experimental information

Characterizations. Scanning electron microscopy (SEM) was performed on Zeiss Sigma500 field emission scanning electron microscope. Transmission electron microscopy (TEM) was operated on JEOL JEM-2200FS. Spherical aberration corrected TEM was operated on Titan Cubed Themis G2300. Nitrogen sorption measurements were conducted on powder samples at 77K using an Autosorb-1 surface area and pore size analyzer (Gemini VII 2390). The specific surface areas were calculated based on the Brunauer Emmett Teller method (BET). X-ray diffraction (XRD) patterns were measured using a Bruker-AXS D8 Advance diffractometer. Raman spectra were recorded on scattering Raman spectrometer of Lanram HR Evo. Ultraviolet-visible (UV-vis) spectra were measured using a Shimadzu UV1800. Fourier transform infrared (FTIR) spectra were obtained by the FTIR spectrometer Nicolet iS10 (Thermo Fisher). The elemental analysis for C, H, and N was conducted on a Vario UNICUBE elemental analyzer using acetanilide as the standard, with oxygen content calculated by difference. Raman spectra were recorded on scattering Raman spectrometer of Lanram HR Evo. X-ray photoelectron spectroscopy (XPS) (Thermo Scientific K-Alpha) was used for the analysis of element/chemical states in the solid samples The X-ray absorption data at the Fe K-edge of the samples were recorded at room temperature in fluorescence mode with 4-element silicon drift detector at BL20U1 (https://cstr.cn/31124.02.SSRF.BL20U1) of the Shanghai Synchrotron Radiation Facility (SSRF). The station was operated with a Si(111) double crystal monochromator. During the measurement, the storage ring was operated at energy of 3.5GeV and a

current of 200 mA (top-up). The photon energy was calibrated with the first inflection point in Fe K-edge of Fe metal foil.

Computational details. All the spin-polarized calculations are performed in the framework of the density functional theory with the projector augmented plane-wave method, as implemented in the Vienna ab initio simulation package [1]. The nuclei-electron and the electron exchange correlation interactions were described by the projector augmented wave (PAW) potentials [2] and the generalized gradient approximation (GGA) [3] with the Perdew-Burke Ernzerh of (PBE) [4] functional, respective. The cut-off energy for plane wave is set to 450 eV. The energy criterion is set to 10−5 eV in iterative solution of the Kohn-Sham equation. A vacuum layer of 15 Å is added perpendicular to the sheet to avoid artificial interaction between periodic images. The Brillouin zone integration is performed using a 3x3x1 k-mesh. All the structures are relaxed until the residual forces on the atoms have declined to less than 0.03 eV/Å. A semi-empirical van der Waals (vdW) correction proposed by Grimme (DFT-D3) [5] was included to account for the dispersion interactions.

The adsorption energies (ΔG) were obtained by

$$\Delta G = \Delta E_{DFT} + \Delta E_{ZPE} - T\Delta S$$

where ΔE_{DFT} is the reaction energy calculated from DFT; ΔE_{ZPE} is the zero-point energy; ΔS is the entropy change.

References in Computational details

[1] Kresse, G.; Joubert, D. From ultrasoft pseudopotentials to the projector augmented-wave method. *Physical Review B* **1999**, *59*, 1758-177.

[2] Blöchl, P. E. Projector Augmented-Wave Method. *Phys. Rev. B* **1994**, *50* (24), 17953-17979

[3] Perdew, J. P.; Burke, K.; Ernzerhof, M. Generalized gradient approximation made simple. *Physical Review Letters* **1996**, *77*, 3865-3868.

[4] Perdew, J. P.; Ernzerhof, M.; Burke, K. Rationale for Mixing Exact Exchange with Density Functional Approximations. *J. Chem. Phys.* **1996**, *105* (22), 9982-9985

[5] S. Grimme, J. Antony, S. Ehrlich, H. Krieg, *J. Chem. Phys.* **2010**, *132*, 154104

Electrochemical measurement. The electrochemical measurements were performed on a CS2350M dual unit electrochemical workstation by using a standard three-electrode cell in the alkaline medium (0.1 M KOH). Hg/HgCl, graphite, and modified glassy carbon electrode (GCE) were used as a reference, counter, and working electrodes, respectively.

The catalyst sample (5 mg) was dispersed in 960 μL of ethanol and 40 μL of Nafion mixture solution by sonication for 1 h. The mixture solution was dropped onto the GC disk with the loading amount of 0.5mg·cm^{-2}.

Cyclic voltammetry (CV) plots were recorded in 0.1 M KOH solution under N_2 or O_2 flow at the potential range of 0-1.2 V. The scan rate was 50 mV·s^{-1}. Linear sweep voltammetry (LSV) plots were recorded at a scan rate of 10 mV·s^{-1} with different rotating speeds (400-2500 rpm) in O_2 saturated 0.1 M KOH aqueous solution with IRs compensations. The potentials measured in this work were calibrated regarding the reversible hydrogen electrode (RHE) through $E_{RHE} = E_{SCE} + 0.059pH + 0.241$.

The exact kinetic parameters, including electron transfer number (n) and kinetic current density (j_k) involved in the typical ORR process, were analyzed based on the Koutecky-Levich (K-L) equation:

$$\frac{1}{j} = \frac{1}{j_k} + \frac{1}{j_L} = \frac{1}{B}\omega^{-\frac{1}{2}} + \frac{1}{j_k}$$

$$B = 0.2nFC_0D_0^{\frac{2}{3}}\nu^{-1/6}$$

In which j, j_L, j_k, are the measured current density, the limiting current density, and the kinetic current density, respectively; ω is the rotation speed in rpm; F is the Faraday constant (96485 C·mol^{-1}); D_0 is the diffusion coefficient of oxygen in 0.1 M KOH (1.90×10^{-5} cm^2·s^{-1}); ν is the kinetic viscosity (0.01 cm^2·s^{-1}); C_0 is the bulk concentration of oxygen (1.2×10^{-6} mol·cm^{-3}).

The electrochemical active surface area was estimated by measuring the electrochemical double-layer capacitance (C_{dl}), which was calculated from cyclic voltammetry (CV) curves recorded within the non-Faradaic region (1.05-1.15 V) at various scan rates ranging from 5 to 30 mV·s^{-1}.

The RRDE test was performed using the RRDE electrode as the working electrode. The ring potential was 1.4V vs RHE. The peroxide species yield of H_2O_2% and the electron transfer number (n) were calculated with the following equations:

$$n = \frac{4\,I_d}{I_d + I_r/N}$$

$$H_2O_2\% = 200\frac{I_r/N}{I_d + I_r/N}$$

Which I_d, disk current; I_r, ring current; N, the current collection efficiency of the Pt ring.

The stability of the catalysts was tested by the chronoamperometric current-time (*i-t*) measurements at a constant potential of 0.5 V vs. reversible hydrogen electrode

(RHE) for 12 hours, and the accelerated durability test under the scan rate of 100 $mV \cdot s^{-1}$ in O_2-saturated 0.1 M KOH solution for 5000 cycles. Methanol tolerance of *i-t* responses was measured with injecting methanol into the electrolyte at 0.55 V vs. RHE

The performance of the homemade setup Zn-air battery was tested by using Fe/N@FMB or Pt/C on carbon paper (1 $mg \cdot cm^{-2}$) as the air cathode, a polished zinc foil as the anode and an aqueous solution of 6 M KOH as the electrolyte. The current-voltage (*I-V*) polarization curves were recorded via the LSV technique at room temperature. Discharge curves of the ZABs were recorded at various current densities, and deep discharge was performed at 20 $mA \cdot cm^{-2}$. The specific capacity of the ZABs was calculated based on the mass of consumed Zn. All tests were conducted in static air without an additional O_2 supply.

Supplementary data

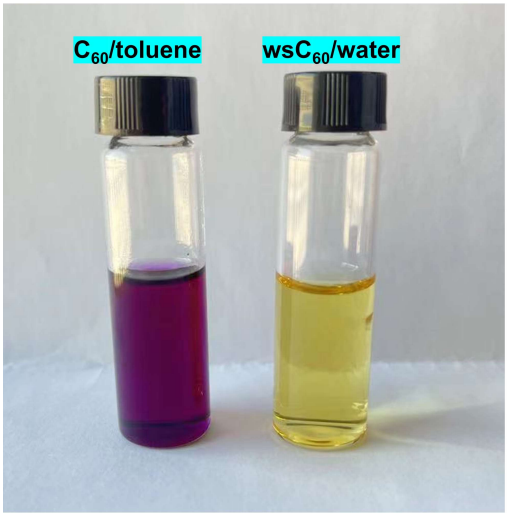

Figure S1. C_{60}s and wsC_{60}s are dissolved in toluene and water, respectively.

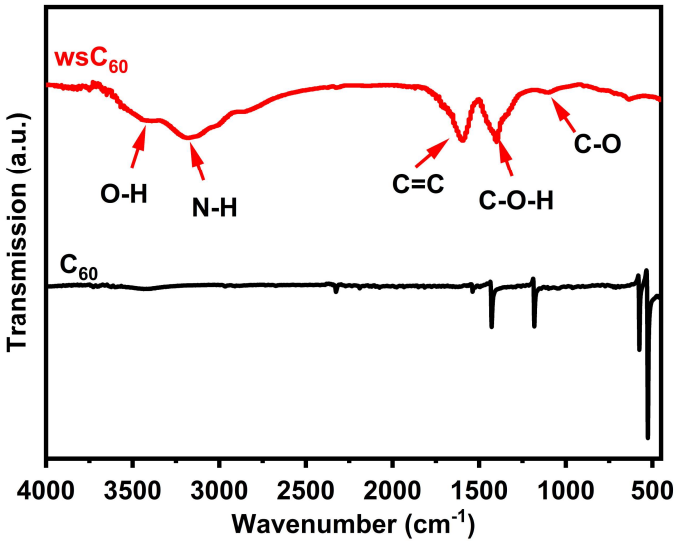

Figure S2. FTIR spectra of C_{60} and wsC_{60}.

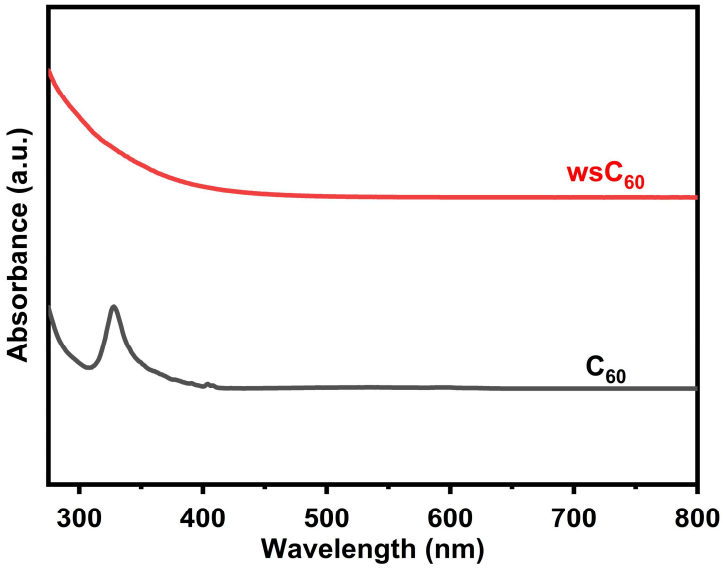

Figure S3. UV-Vis spectra of C_{60} and wsC_{60}

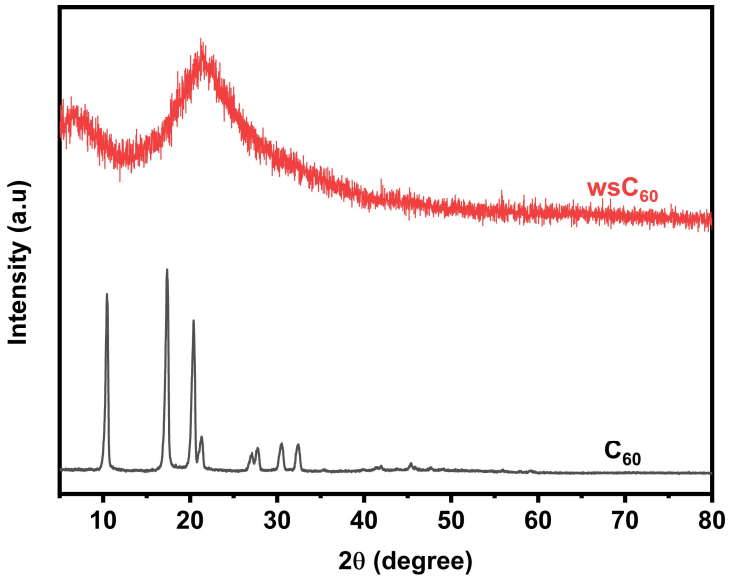

Figure S4. XRD spectra of C_{60} and wsC_{60}.

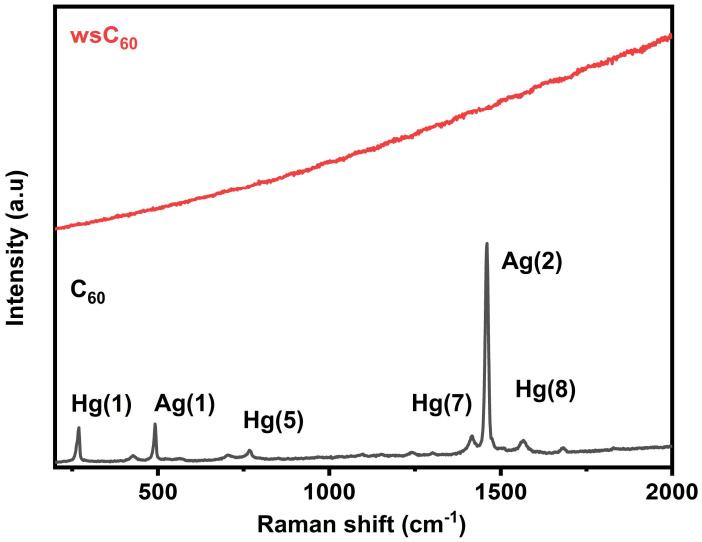

Figure S5. Raman spectra of C_{60} and wsC_{60}.

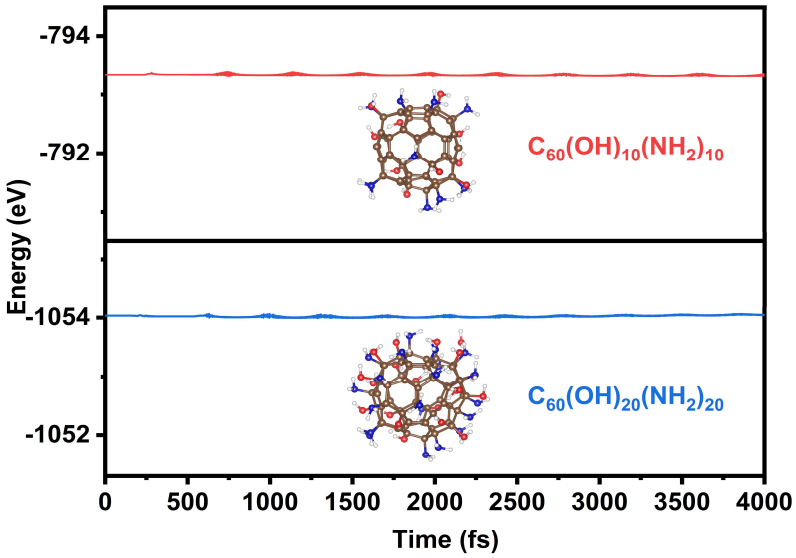

Figure S6. Optimized equilibrium structures of C_{60} grafted with different numbers of -OH and -NH_2 groups ($C_{60}(OH)_{10}(NH_2)_{10}$ and $C_{60}(OH)_{20}(NH_2)_{20}$) and their corresponding potential energy evolution during the 4000-fs AIMD simulation at 300 K. The total energy fluctuation is confined within 0.1 eV, indicating excellent thermal stability of the functionalized structures. It demonstrates that the characteristic buckyball curvature and the grafted functional groups are well preserved without structural collapse.

Table S1. The content of C, O, N and H of wsC_{60} from elemental analysis

Sample	C (wt.%)	O (wt.%)	N (wt.%)	H (wt.%)
wsC_{60}	31.82	49.88	12.96	5.34

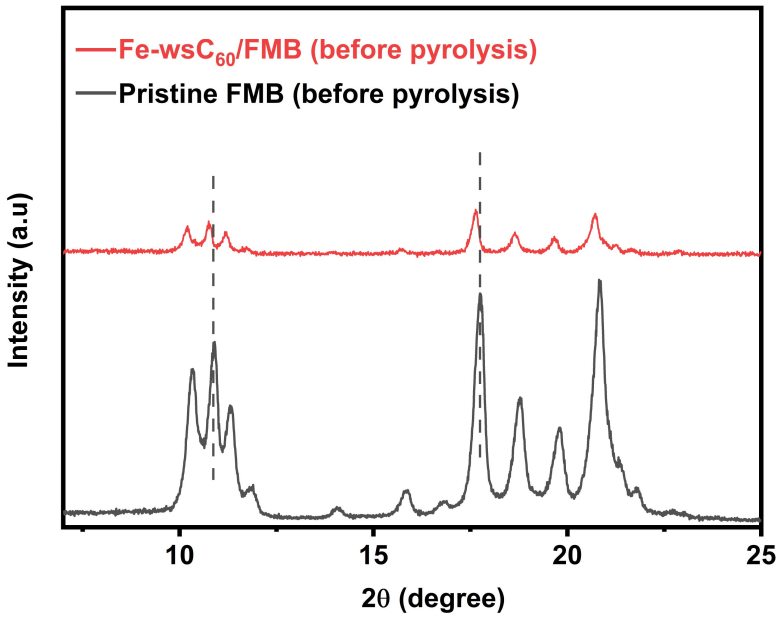

Figure S7. XRD spectra of Pristine FMB (before pyrolysis) and Fe-wsC_{60}/FMB (before pyrolysis).

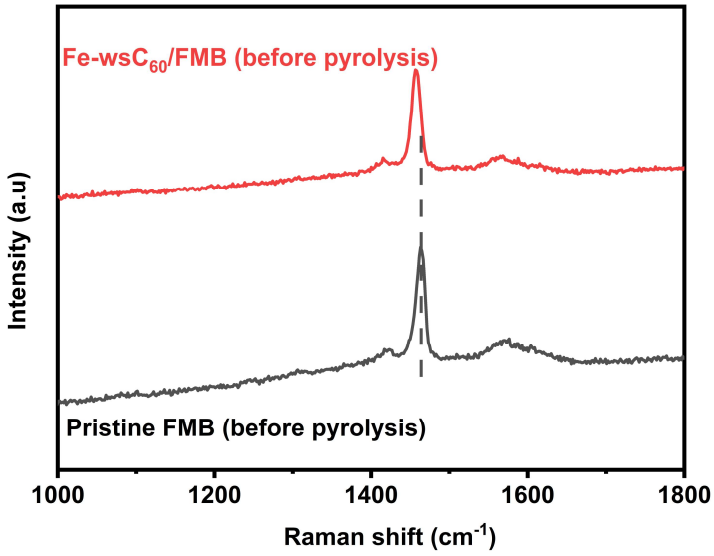

Figure S8. Raman spectra of pristine FMB (before pyrolysis) and Fe-wsC_{60}/FMB (before pyrolysis).

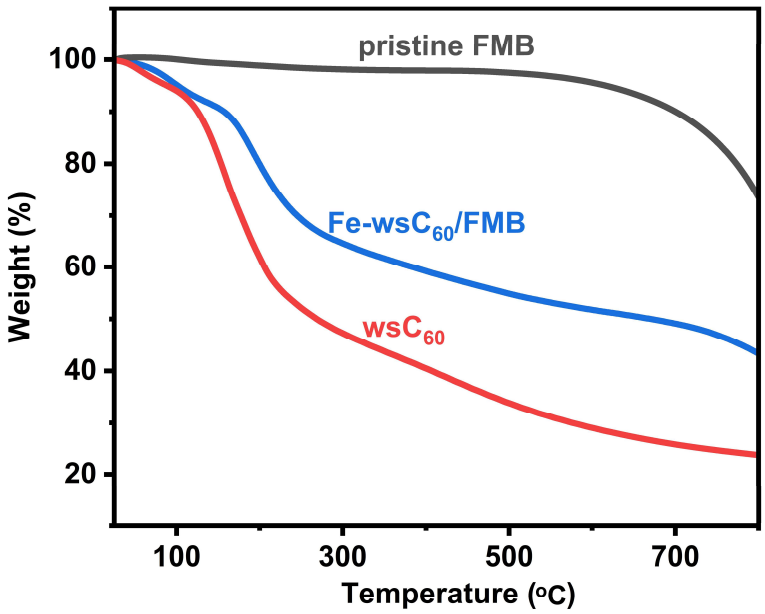

Figure S9. Thermogravimetric analysis for pristine FMB, wsC_{60} and the Fe-wsC_{60}/FMB composite.

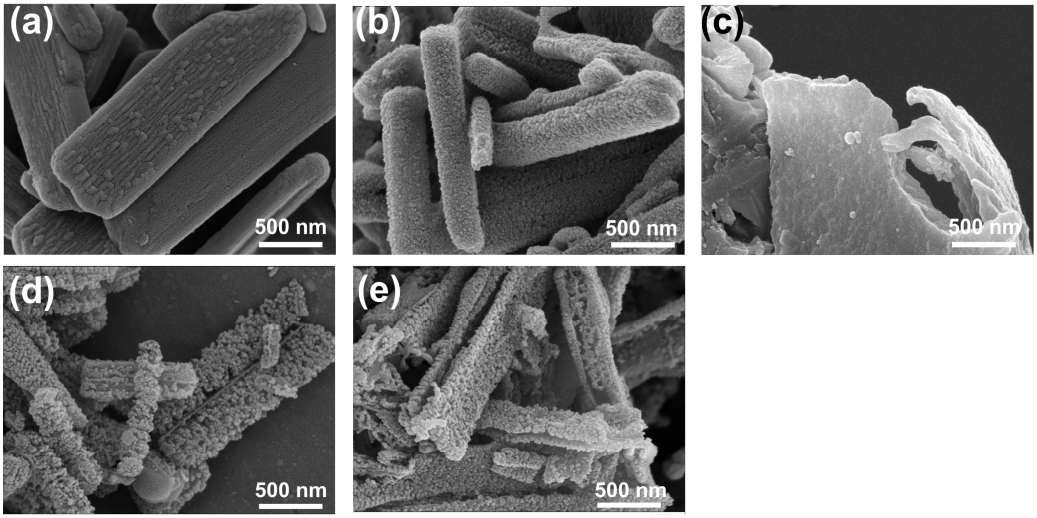

Figure S10. SEM images of (a) pristine FMB (before pyrolysis), (b) FMB after pyrolysis, (c) Fe@wsC_{60} (without FMB host), (d) N@FMB, and (e) Fe/N@FMB.

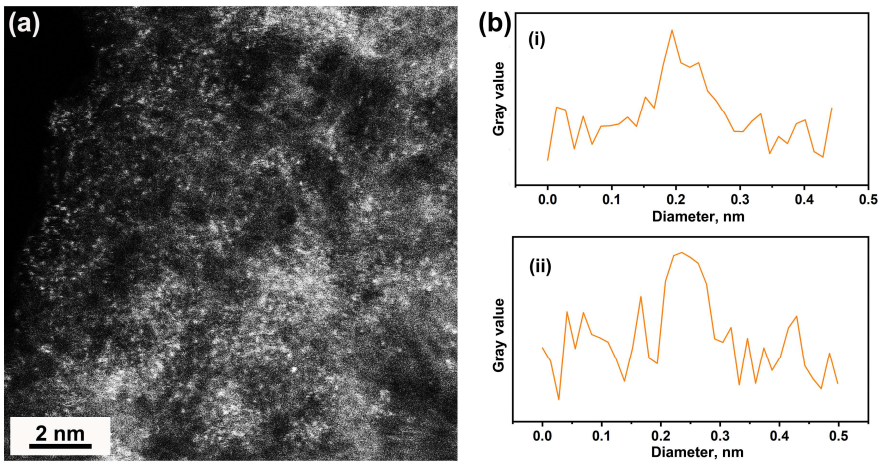

Figure S11. (a) HAADF-STEM image of Fe/N@FMB, and (b) the intensity line profiles across two dots in (a).

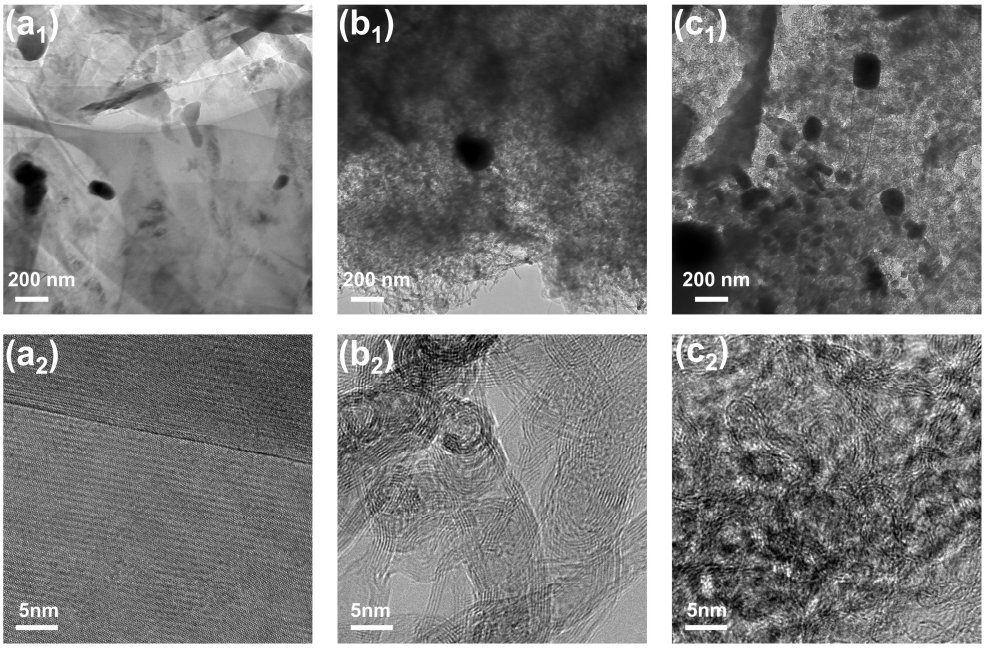

Figure S12. TEM images of (a_1) Fe/N@GR, (b_1) Fe/N@CNT and (c_1) Fe/N@KB; HRTEM images of (a_2) Fe/N@GR, (b_2) Fe/N@CNT and (c_2) Fe/N@KB.

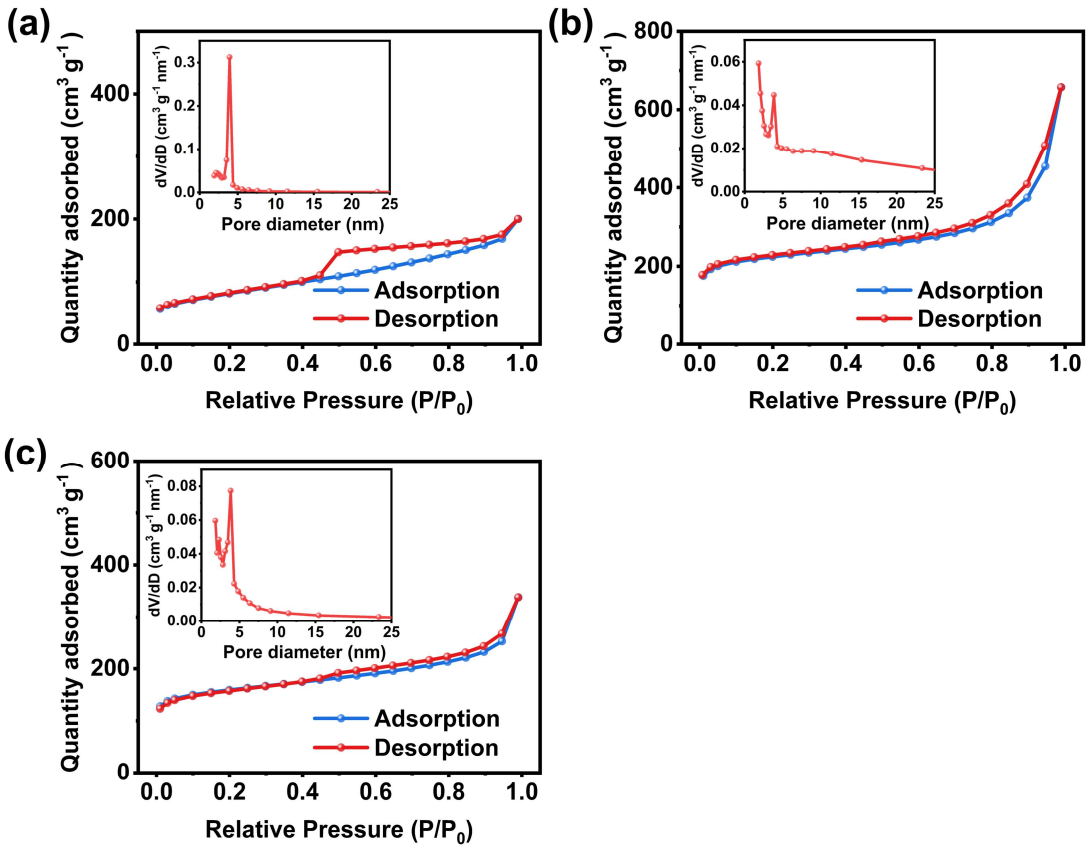

Figure S13. Nitrogen adsorption-desorption isotherms and pore size distributions of (a) Fe@wsC$_{60}$, (b) N@FMB and (c) FMB.

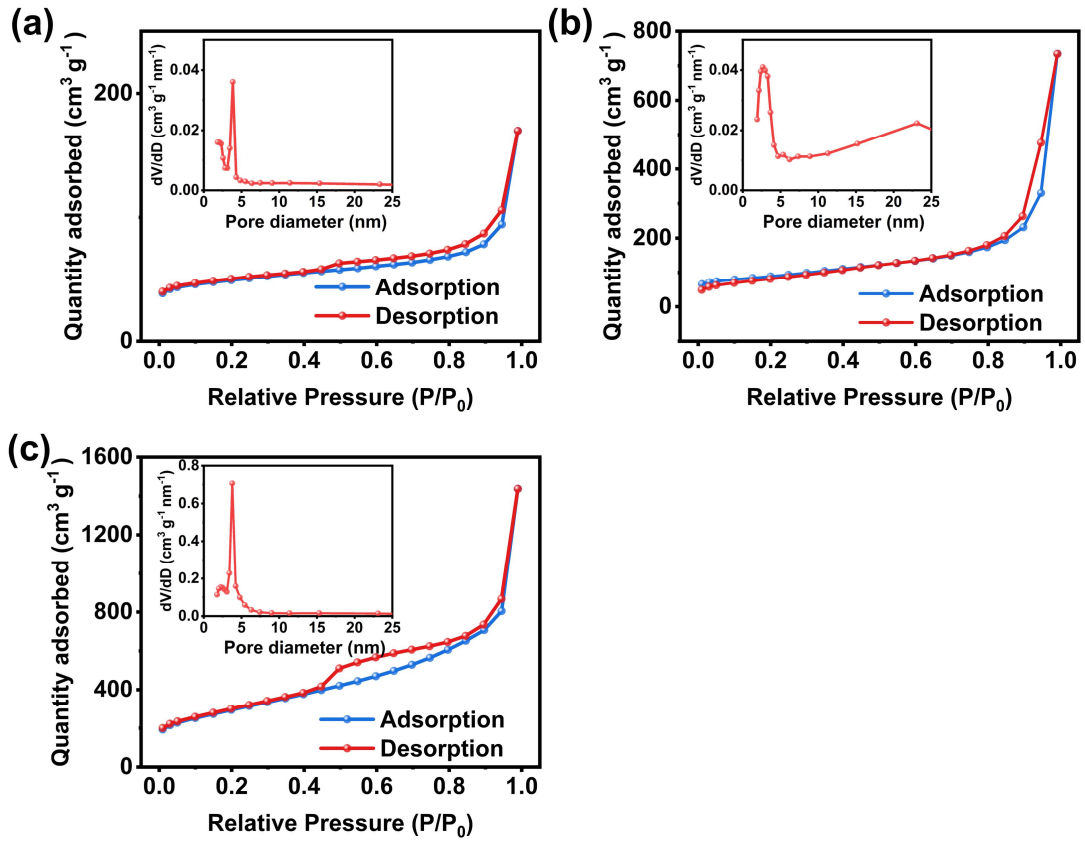

Figure S14. Nitrogen adsorption-desorption isotherms and pore size distributions of (a) Fe/N@GR, (b) Fe/N@CNT, and (c) Fe/N@KB.

Table S2. The porous features of the prepared carbon samples from N_2 sorption measurement

Sample	Specific surface area ($m^2\ g^{-1}$)	Pore volume ($m^3\ g^{-1}$)	Average pore diameter (nm)
FMB	513.35	0.39	6.43
Fe@wsC_{60}	282.46	0.32	4.36
N@FMB	722.33	0.81	10.59
Fe/N@FMB	535.62	0.78	10.21
Fe/N@GR	161.03	0.23	10.36
Fe/N@CNT	303.94	1.13	15.01
Fe/N@KB	1039.25	2.26	7.77

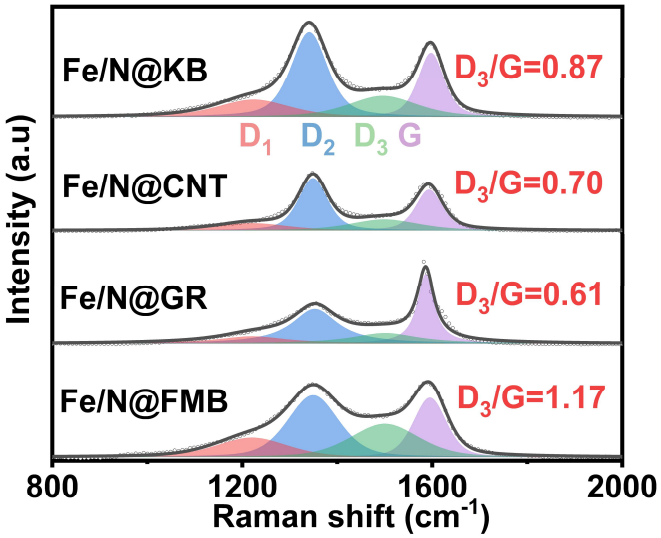

Figure S15. Raman spectra of Fe/N@FMB, Fe/N@GR, Fe/N@CNT and Fe/N@KB.

Table S3. The elemental compositions and contents of N@FMB, Fe@wsC60, Fe/N@FMB, Fe/N@GR, Fe/N@CNT and Fe/N@KB from XPS results

Sample	C (at.%)	O (at.%)	N (at.%)	Fe (at.%)
N@FMB	92.35	5.24	2.41	
Fe@wsC$_{60}$	89.68	7.04	2.78	0.49
Fe/N@FMB	91.20	6.43	2.10	0.28
Fe/N@GR	94.79	3.59	1.38	0.25
Fe/N@CNT	95.92	2.47	1.43	0.18
Fe/N@KB	93.61	4.58	1.59	0.21

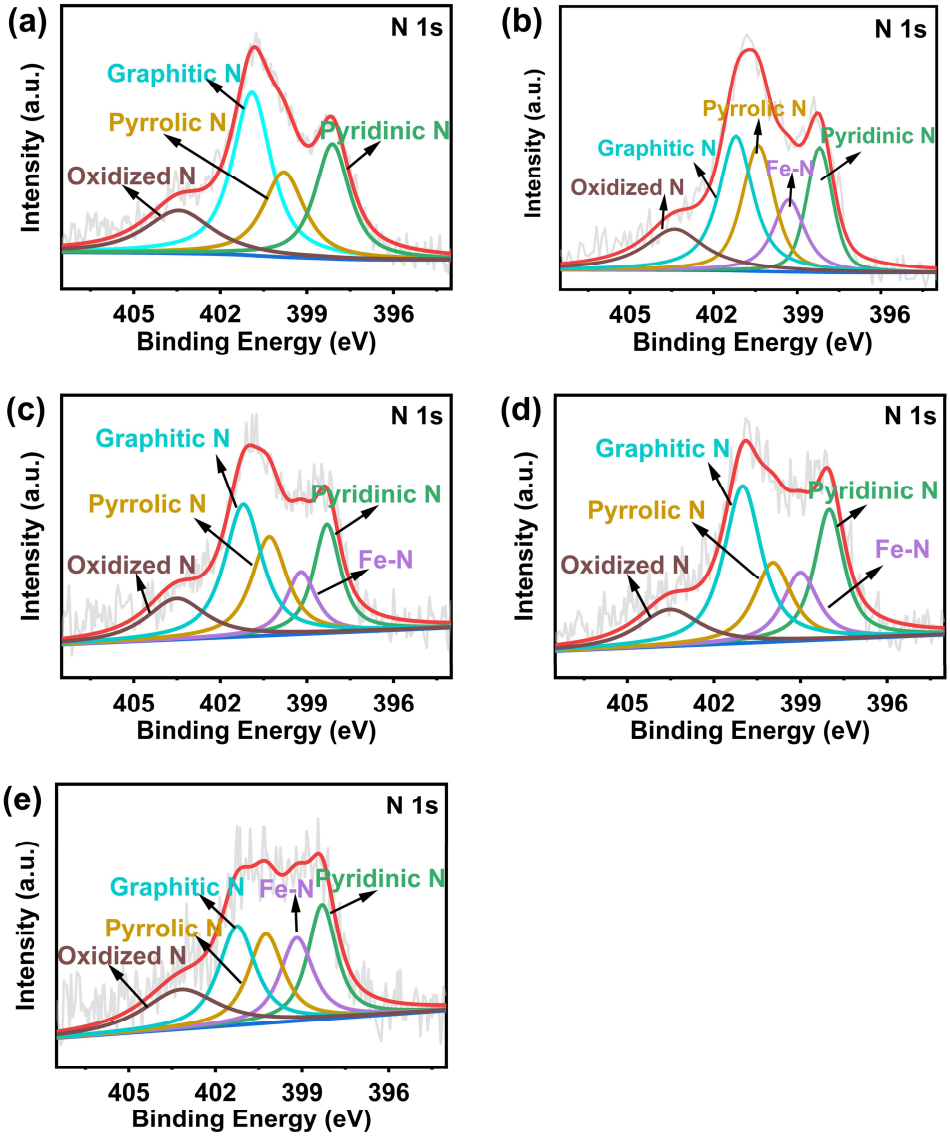

Figure S16. The N 1s spectra of (a) N@FMB, (b) Fe@wsC_{60}, (c) Fe/N@GR, (d) Fe/N@CNT, and (e) Fe/N@KB.

Table S4. The relative content and type of N in N@FMB, Fe@wsC60, Fe/N@FMB, Fe/N@GR, Fe/N@CNT, and Fe/N@KB calculated based on XPS results

Sample	pyridinic N	Fe-N	pyrrolic N	graphitic N	oxidized N
N@FMB	23.87%		20.93%	38.14%	17.06%
Fe@wsC$_{60}$	17.53%	14.14%	23.07%	28.66%	16.60%
Fe/N@FMB	24.10%	23.30%	19.19%	20.48%	12.93%
Fe/N@GR	18.84%	11.76%	22.35%	31.74%	15.31%
Fe/N@CNT	22.18%	13.67%	17.09%	34.14%	12.92%
Fe/N@KB	20.93%	17.59%	19.88%	23.15%	18.45%

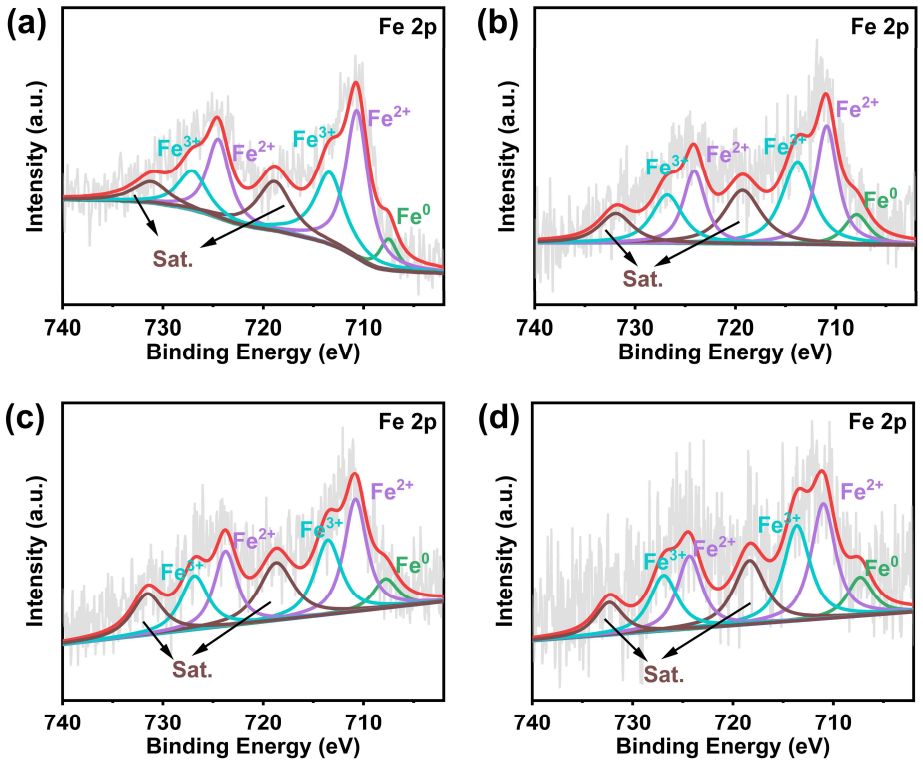

Figure S17. The Fe 2p spectra (a) Fe@wsC$_{60}$, (b) Fe/N@GR, (c) Fe/N@CNT, and (d) Fe/N@KB.

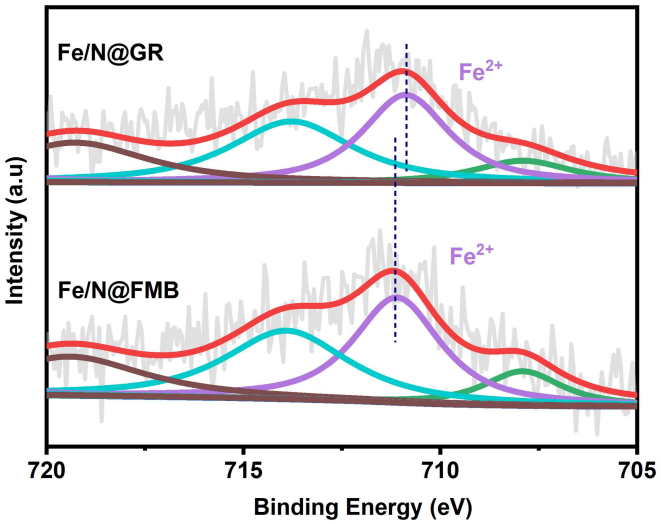

Figure S18. Comparative analysis for the Fe $2p_{3/2}$ spectral region of Fe/N@FMB and Fe/N@GR in the Fe 2p XPS spectra.

Table S5. The relative contents of Fe^{2+} and Fe^{0} in Fe/N@FMB, Fe/N@GR, Fe/N@CNT, and Fe/N@KB based on XPS analysis.

Sample	Fe/N@FMB	Fe/N@GR	Fe/N@CNT	Fe/N@KB
Fe^{2+}	45.13%	43.80%	48.32%	44.07%
Fe^{0}	13.23%	12.68%	13.66%	15.62%
Fe^{2+}: Fe^{0}	3.41	3.45	3.54	2.82

Table S6. The Fe content of Fe/N@FMB, Fe/N@GR, Fe/N@CNT and Fe/N@KB by ICP-OES

Sample	Fe/N@FMB	Fe/N@GR	Fe/N@CNT	Fe/N@KB
Fe (wt.%)	5.51	3.26	3.84	3.34

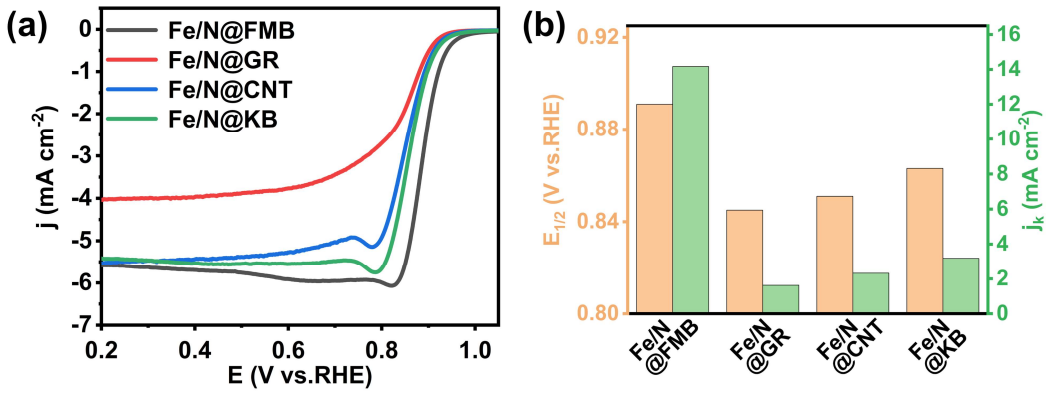

Figure S19. (a) LSV curves of Fe/N@FMB, Fe/N@GR, Fe/N@CNT, and Fe/N@KB at a rate of 10mV s^{-1} at 1600 rpm. (b) $E_{1/2}$ and the comparison of jK at 0.875 V and $E_{1/2}$ of Fe/N@FMB, Fe/N@GR, Fe/N@CNT, and Fe/N@KB.

Table S7. ORR activities of FMB, N@FMB, Fe@wsC60, Fe/N@FMB, Fe/N@GR, Fe/N@CNT, Fe/N@KB, and Pt/C

Sample	E_0 (V)	$E_{1/2}$ (V)	j_L(mA·cm^{-1})
FMB	0.811	0.716	3.67
N@FMB	0.919	0.832	4.89
Fe@wsC$_{60}$	0.937	0.843	4.08
Fe/N@FMB	0.994	0.891	5.59
Fe/N@GR	0.942	0.845	4.03
Fe/N@CNT	0.955	0.851	5.53
Fe/N@KB	0.965	0.863	5.41
Pt/C	0.973	0.863	5.27

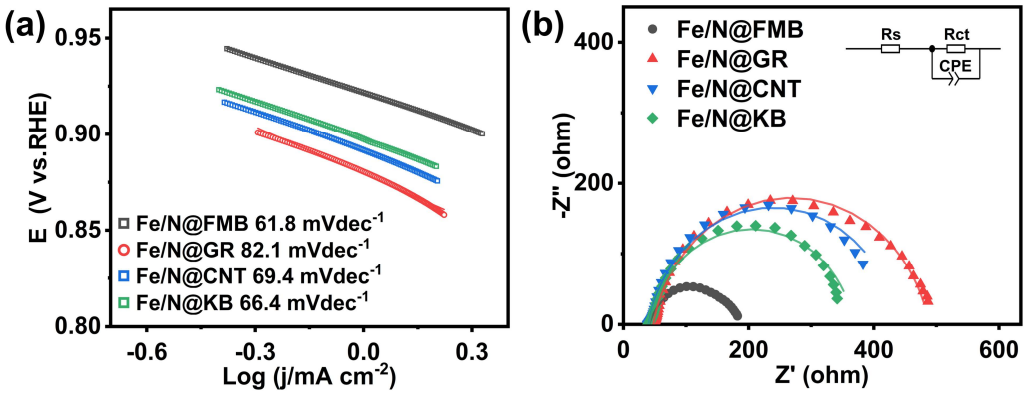

Figure S20. (a) Tafel plots of Fe/N@FMB, Fe/N@GR, Fe/N@CNT, and Fe/N@KB.

(b) Nyquist plots of Fe/N@FMB, Fe/N@GR, Fe/N@CNT, and Fe/N@KB.

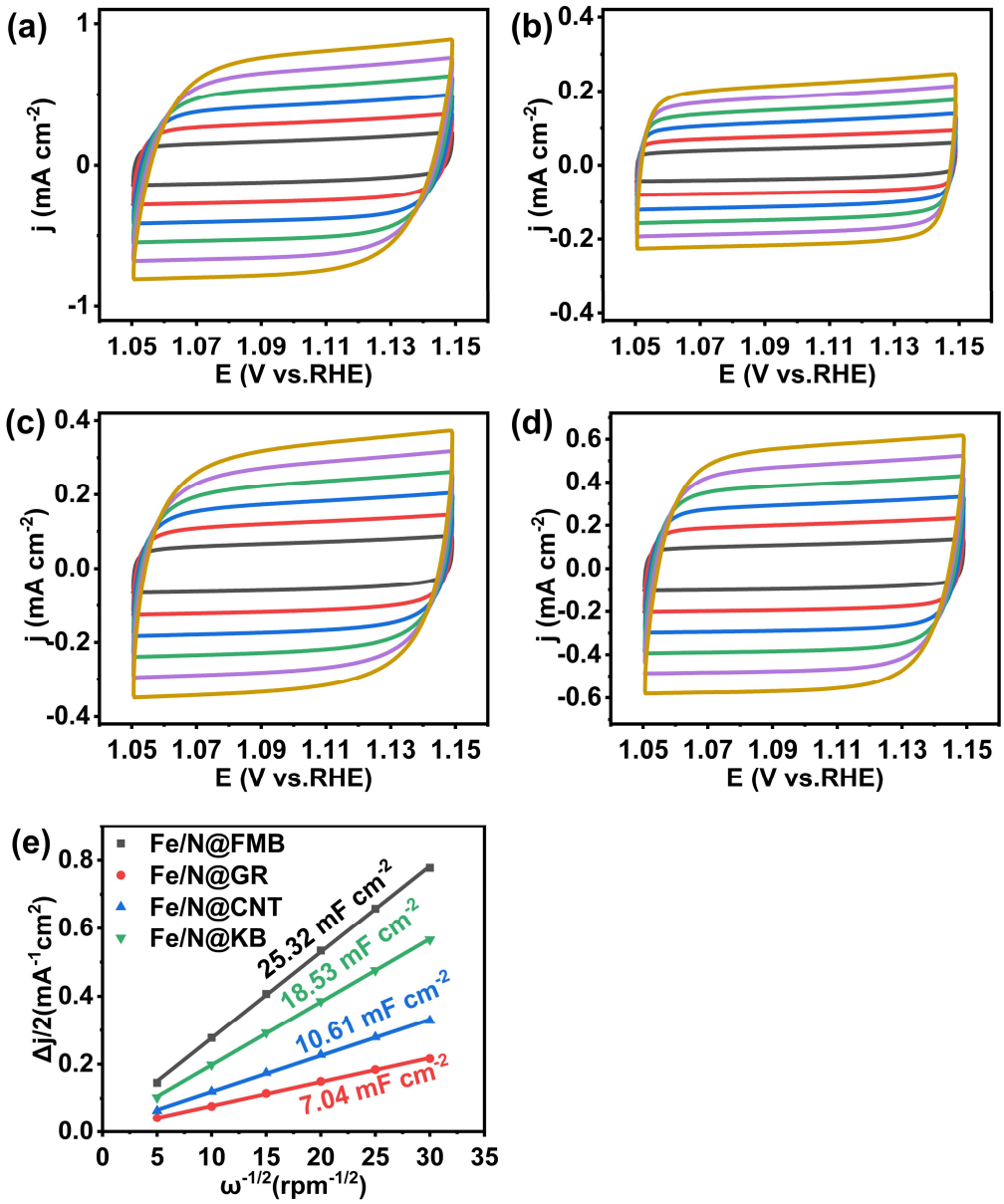

Figure S21. CV curves of (a) Fe/N@FMB, (b) Fe/N@GR, (c) Fe/N@CNT and (d) Fe/N@KB in the non-Faradaic potential range of 1.05-1.15 V at the scan rate of 5-30 mV s^{-1}. (d) Double-layer capacitance (C_{dl}) of Fe/N@FMB, Fe/N@GR, Fe/N@CNT and Fe/N@KB.

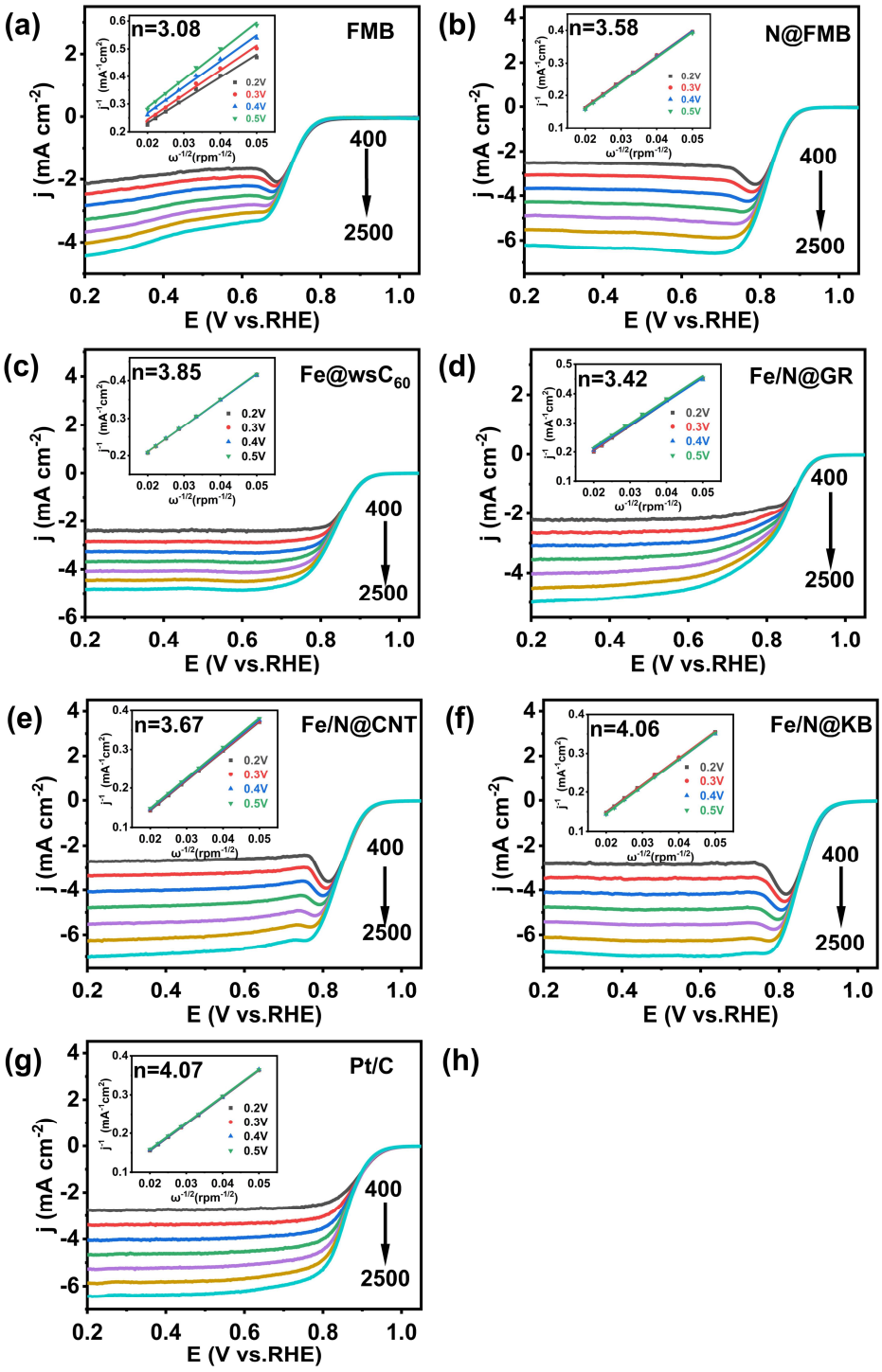

Figure S22. LSV curves of (a) FMB, (b) N@FMB, (c) Fe@wsC$_{60}$, (d) Fe/N@GR, (e) Fe/N@CNT, (f) Fe/N@KB, and (g) commercial Pt/C at rotation speeds from 400 to 2500 rpm. (Insets: corresponding K-L plots at 0.2-0.5 V and electron transfer number (n).

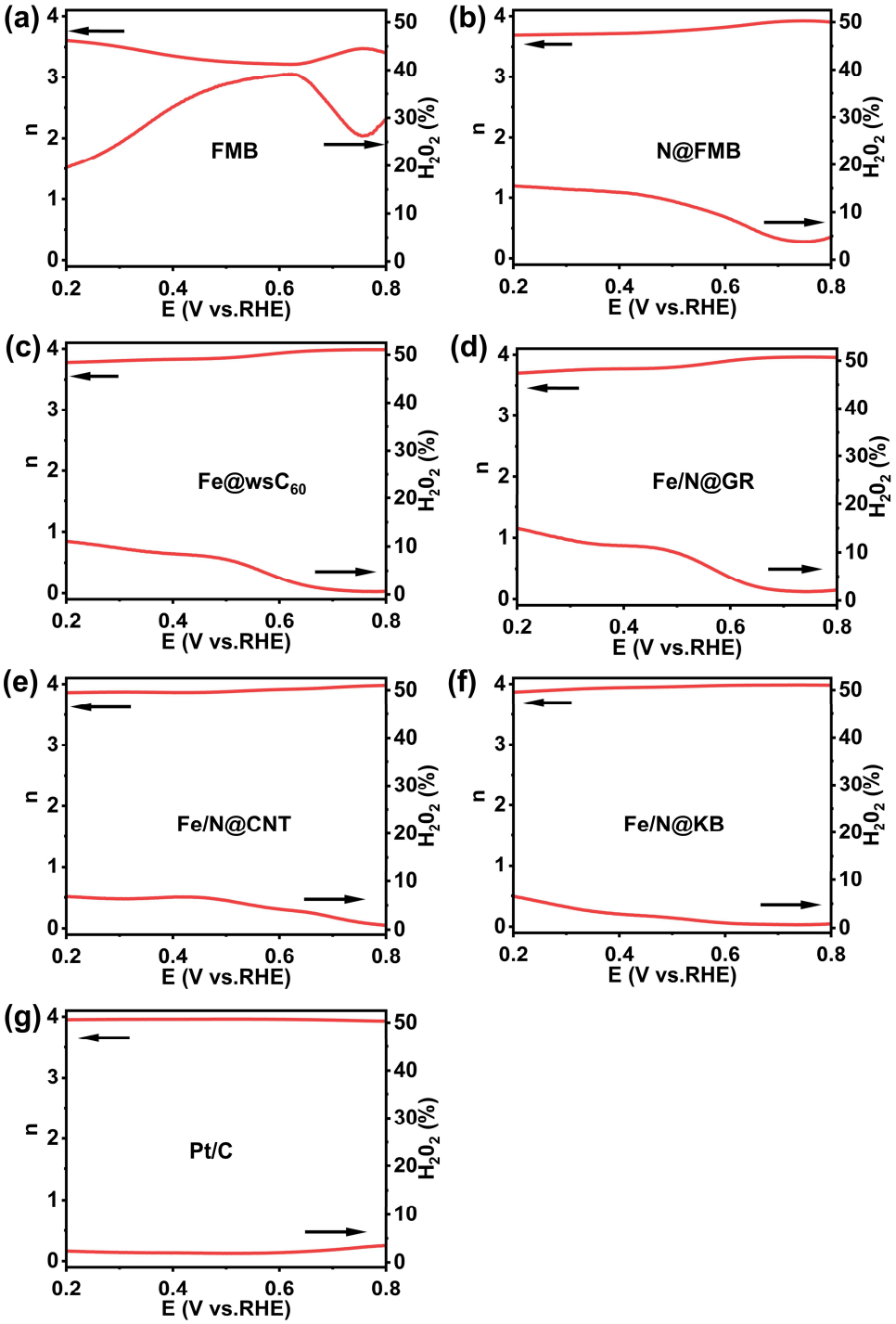

Figure S23. H_2O_2 yield and n of (a) FMB, (b) N@FMB, (c) Fe@wsC$_{60}$, (d) Fe/N@GR, (e) Fe/N@CNT, (f) Fe/N@KB, and (g) Pt/C from RRDE measurements.

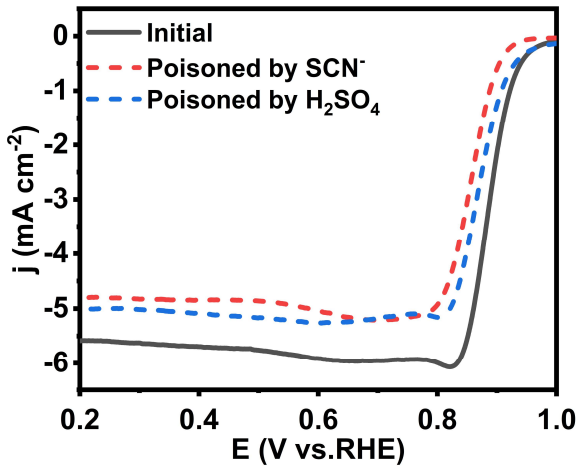

Figure S24. LSV curves of Fe/N@FMB before and after H_2SO_4 (0.5M) and KSCN (0.01M) chemical treatment. The measurements were conducted in O_2-saturated 0.1 M KOH at a rotation rate of 1600 rpm with a scan rate of 10 $mV \cdot s^{-1}$.

Table S8. A comparative summary of key metrics for Fe/N@FMB and other advanced Fe-N-C catalysts in zinc-air batteries

catalyst	curved/ planar	$E_{1/2}$(V)	open-circuit voltage (V)	power density (mW·cm^{-2})	Ref.
Fe/N@FMB	curved	0.89	1.49	173.3	This work
T-Fe SAC	curved	0.91	1.52	199	Y. Zhu, et al., *Angew. Chem. Int. Ed.*, 2024, **63**, e202319370
FePc/CNO	curved	0.89	1.44	162.4	L. Li, et al., *Nano Lett.*, 2025, **25**, 16459
Fe/CCNs-P123	curved	0.89	1.49	162.7	J.-K. et al., *Adv. Sci.*, 2025, **12**, 2412387.
Fe_3C/FeN@CNT-900	planar	0.89	1.46	145.5	T. Zhi, et al., *Small*, 2025, **21**, e08558.
Fe-N-C/Fe_3C-op	planar	0.91	1.57	137.4	J. Chang, et al., *Adv. Sci.*, 2023, **10**, 2301656.
Fe_3C/N,S-CNS	planar	0.86	1.43	163	Q.-D. Ruan, et al., *Small*, 2023, **19**, 2300136.
Fe/Fe_3C/$FeN_{0.0324}$@N-GC-850	planer	0.87	1.52	101.6	G. Li, et al., *Chem. Eng. J.*, 2023, **451**, 13882
Fe_3C@NPW	planer	0.87	1.48	125	M. Cao, et al., *Small*, 2022, **18**, 2202014.

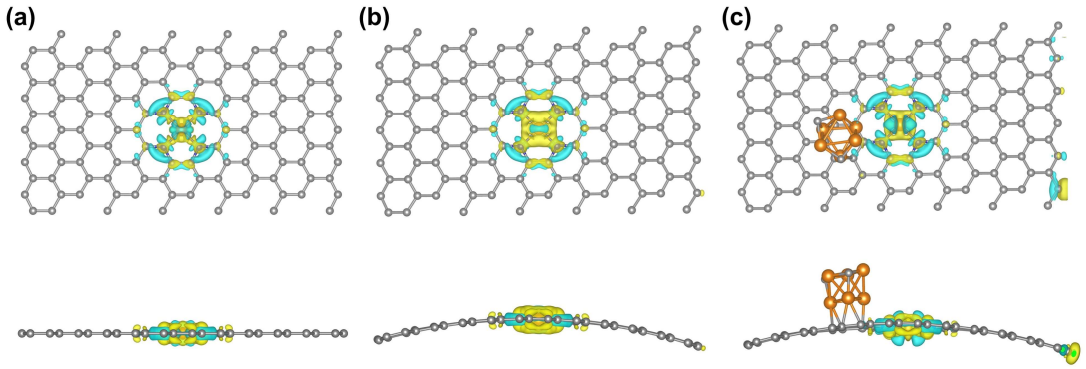

Figure S25. Charge density difference diagrams of (a) Fe-N_4, (b) C-Fe-N_4, (c) C-Fe-N_4/Fe_3C

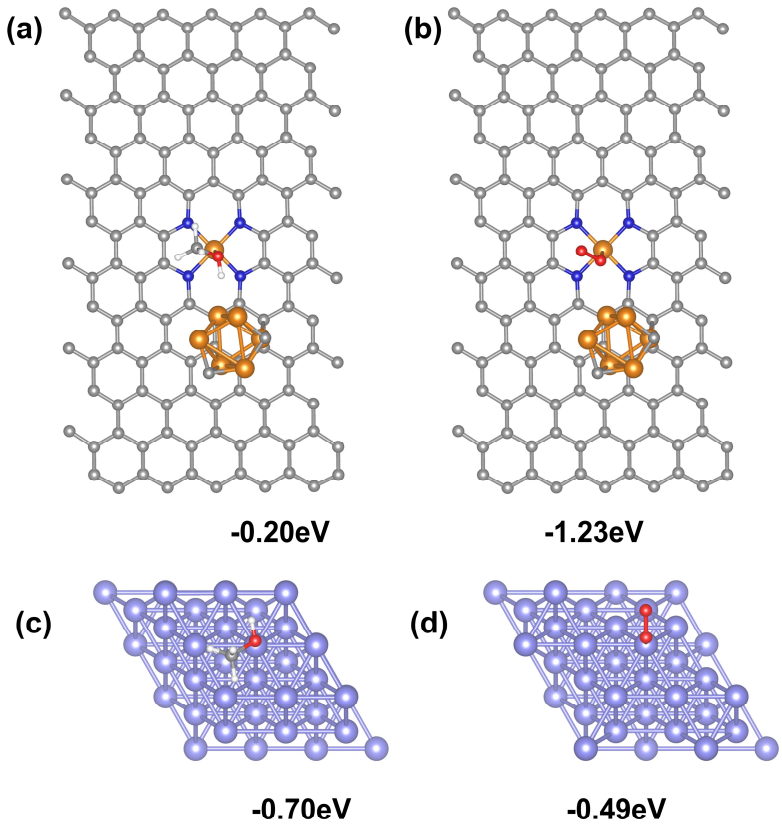

Figure S26. Comparative adsorption modes and energies of methanol (MeOH) and O_2 at C-Fe-N_4/Fe_3C and Pt.